



Effect of cycling rate, particle size and transport properties on lithium-ion cathode performance

Wenbo Du^a, Amit Gupta^a, Xiangchun Zhang^b, Ann Marie Sastry^{b,c,d}, Wei Shyy^{a,*}

^a Department of Aerospace Engineering, University of Michigan, Ann Arbor, MI 48109, USA

^b Department of Mechanical Engineering, University of Michigan, Ann Arbor, MI 48109, USA

^c Department of Materials Science and Engineering, University of Michigan, Ann Arbor, MI 48109, USA

^d Department of Biomedical Engineering, University of Michigan, Ann Arbor, MI 48109, USA

ARTICLE INFO

Article history:

Received 5 November 2009

Accepted 4 March 2010

Available online 4 May 2010

Keywords:

Lithium-ion battery

Surrogate modeling

Porous electrode model

Global sensitivity analysis

Diffusion coefficient

ABSTRACT

Much progress has been made in modeling the lithium-ion battery technology. There exists a critical need to establish a framework to assess the role of various physical, geometrical, and operating parameters and their relative influence on the energy and power capability of batteries. In this study, a surrogate modeling framework has been introduced to map the effect of design-related parameters on the performance of a lithium-ion cell. In particular, the effects of cycling rate, cathode particle size, and diffusion coefficient and electrical conductivity of the solid cathode material, on the specific energy and power have been studied using a cell-level model in conjunction with tools such as kriging, polynomial response, and radial-basis neural networks. Through global sensitivity analysis the relative impact of the various parameters are quantified under different scenarios. Specifically, the design space can be split into distinct regions based on the discharge and diffusion time scales for separate, more refined analysis. It is shown that the cathode performance becomes independent of the diffusion coefficient above a critical value. A Pareto-optimal front was constructed to quantify the tradeoff between maximum achievable energy and power levels. Such an analysis can provide guidelines for the optimization of the positive electrode design.

© 2010 Elsevier Ltd. All rights reserved.

1. Introduction

The successful development and implementation of high-energy lithium-ion batteries [1–3] in recent years has allowed for their use in a variety of portable devices. Li-based batteries offer significant advantage over other technologies due to their high energy density and high voltage. The extension of such energy systems from portable electronics to hybrid and electric vehicles is not trivial, as the number of design variables increases enormously which can only be analyzed at a reasonable cost in a proper mathematical framework. For their successful implementation, the effects of both material properties and morphology need to be considered in a physics-based model. The role of material selection, discharge rate, and design parameters such as the electrode particle size on battery performance are still not well understood. This in part could be attributed to the disparity in the measurement of the material properties, such as diffusivity and electronic conductivity in solid particles, recorded in the experiments conducted by several groups over the past two decades. For instance, estimates of the diffusion coefficient are highly sensitive to uncer-

tainties in measurements of the true cross-sectional surface area for the insertion process, as well as the technique used [4]. Experiments conducted by various groups [4–10] to study these effects have resulted in time consuming and difficult analyses of the cell performance due to the limitations of the manufacturing process for tuning the design parameters.

Theoretical analysis and computer simulations of the intercalation/deintercalation process in lithium-ion batteries offer an attractive alternative and have been gaining widespread attention [11–22]. Different mathematical formulations, such as the single-particle [11] and porous-electrode models [12], have been employed to estimate the transport and kinetic parameters for a carbon–LiCoO₂ cell for different rates of discharge [13]. However, the single-particle model was only valid up to a rate of 1C as it failed to predict cell behavior at higher rates. Paxton and Newman [14] have proposed a theoretical approach for estimating a constant value of the diffusion coefficient by examining the behavior in a single-particle in a system where the diffusion coefficient is a strong function of the state of charge; this methodology was formulated and implemented for a nickel oxide electrode. Arora et al. [15] have outlined a procedure for including the effect of capacity fading as a result of side reactions into the porous-electrode model. Zhang et al. [16] have proposed a mathematical model capable

* Corresponding author.

E-mail address: weishyy@umich.edu (W. Shyy).

Nomenclature

a	vector of radial-basis functions	S_{Ti}	total factor global sensitivity index for <i>i</i> th design variable
b	coefficients of linear combinations for polynomial regression and kriging	t	time (s)
c_1	concentration of Li-ions in the solid (mol/m ³)	t_+^0	cation transference number
c_2	concentration of Li-ions in the liquid (mol/m ³)	t_{dif}	characteristic diffusion time (s)
D_s	diffusion coefficient in the solid phase (m ² /s)	t_{dis}	discharge time (s)
D_2^{eff}	effective diffusivity in the liquid (m ² /s)	T	temperature (K)
$E(\cdot)$	expected value of the quantity	U_{OCP}	open-circuit potential (V)
f_a	activity coefficient	$V(\cdot)$	variance of the quantity
F	Faraday's constant (C/mol)	w_i	coefficient of linear combinations in radial-basis functions
$i_{0,j}$	exchange current density (A/m ²)	X	$N_S \times N_{PRG}$ Gramian matrix of basis functions
i_2	current through the separator (A/m ²)	y	true function to be modeled
$i_{n,n}$	current density in the anode (A/m ²)	y	vector of responses at sampled design points
$i_{n,p}$	current density in the cathode (A/m ²)	y_i	response at <i>i</i> th design point
I_{dis}	discharge current (A/m ²)	$\alpha_{a,j}$	transfer coefficient in the anode
J	volumetric reaction current (A/m ³)	$\alpha_{c,j}$	transfer coefficient in the cathode
k	reaction rate parameter (m ^{5/2} /mol ^{1/2} -s)	β	radial-basis spread coefficient
n	number of electrons transferred in electrode reaction	δ_n	thickness of the anode (negative electrode) (m)
N_{PRG}	number of terms in polynomial regression	δ_p	thickness of the cathode (positive electrode) (m)
N_{RBF}	number of radial-basis functions	δ_s	thickness of the separator (m)
N_S	number of sampled design points	$\varepsilon_{1,n}$	porosity in the anode
r	radial coordinate (m)	$\varepsilon_{1,p}$	porosity in the cathode
R	universal gas constant (J/K-mol)	φ_1	potential in the solid phase (V)
R_{adj}^2	adjusted coefficient of multiple determination	φ_2	potential in the liquid phase (V)
$R_{s,n}$	radius of anode particles (m)	η_j	surface overpotential of the cell (V)
$R_{s,p}$	radius of cathode particles (m)	κ	effective ionic conductivity in the liquid phase (S/m)
s_i	stoichiometric coefficient of species <i>i</i>	σ	effective electronic conductivity of the solid phase (S/m)
S_{Mi}	main factor global sensitivity index for <i>i</i> th design variable	τ	dimensionless time

of including the mass transport within the particle and kinetics at the particle–electrolyte interface to simulate lithium intercalation in a spinel particle. Results were quantified in terms of the ratio of the diffusional resistance of lithium in the solid to the interfacial kinetic resistance. A larger value of this ratio indicated a faster interfacial charge transfer, and a lower value a faster diffusion of lithium in the solid. Arora et al. [10] have modeled lithium-ion polymer cells with different electrode thicknesses, initial salt concentrations and higher material loadings. Using a rate-dependent salt diffusion coefficient, good agreement between theory and experiments was shown. The solution-phase diffusion limitations were the limiting factor for high-rate discharges, based on experiments and model predictions. It was shown that at higher discharge rates even a small change in the solid diffusion coefficient led to significant changes in the discharge profile. Nagarajan et al. [17], through a mathematical model to study the effect of particle size distribution (PSD) on the discharge behavior of intercalation electrode systems, have shown that the electrode utilization could be potentially increased by using a binary mixture of small and large particles. Doyle and Fuentes [18] have shown that diffusion inside the graphite electrode is affected marginally by the concentration polarization that occurs inside the electrode. Recently, significant attention has been directed towards microscopic-scale modeling of the electrode structure to investigate the role of particle aggregation on maximum achievable power densities [19]. The total capacity and power density of the battery was shown to diminish with decreasing diffusivity. The specific power and energy did not change for diffusion coefficient smaller than 1×10^{-11} cm²/s, as the Ragone curves reached an asymptotic response. A homogenous, small, well-dispersed particle size distribution was shown to result in higher power densities and more effective active material utilization. Using particle-scale models, Zhang et al. [20,21] have simulated intercalation-induced stresses

in ellipsoidal particles [20], and heat generation and intercalation-induced stress inside spherical and ellipsoidal LiMn₂O₄ particles together with surrogate-based analysis [21]. It was shown that larger particles and higher discharge rates lead to higher intercalation-induced stresses in LiMn₂O₄ electrodes. In addition, intercalation-induced stress and heat generation increased with increasing equivalent particle size and potential sweep rate.

Potential opportunities for manipulating the morphology of the particle clusters comprising lithium-ion electrodes to attain performance goals would only be possible by developing a better understanding of the role of material properties and operating conditions on battery performance. In spite of significant modeling effort, the role of process variables (such as particle size, solid-state diffusivity and electrical conductivity) on the performance of lithium-ion batteries is still not well understood. In addition, the maximum energy that a battery can provide is dependent on the discharge rate required by its application. To identify the role of such a large number of factors that influence the battery performance, large scale simulations of a complete battery pack that consider the microstructure would be required, which inherently would be computationally intensive and expensive. An alternative and parallel method is to rely on physics-based macroscopic models to simulate the cell performance with respect to various design variables and construct reduced-order models that offer fast prediction with respect to design variables. Surrogate-based analysis tools offer one such option, as they can be used to systematically organize the simulations to represent the entire design space, provide fast prediction of system response to the variables through model estimation (such as kriging (KRG), polynomial regression (PRS), and radial-basis functions (RBNN)) and appraisal, identify critical regions where performance is good or poor, and perform sensitivity analysis to compare the relative importance of the design variables. Previously, surrogate modeling has been employed for a variety of

applications, including design optimization for subsonic diffusers [22] and particle shape and size selection in conjunction with micro-scale modeling of lithium-ion electrodes [21]. Since surrogate tools have not been applied to battery cells, we set the following objectives in the present work:

- (1) Build on prior work in physics-based modeling of battery cells containing porous electrodes to create scalable physical models that are capable of incorporating both materials properties (for example, diffusivity and conductivity) and morphology (for example, particle size and shape) into simulations of battery performance.
- (2) Develop surrogate-based analytical tools to identify local optima in performance based on physics-based modeling, and conduct cross-validation studies of alternative surrogates and to identify optimal design scenarios between power and energy.
- (3) Use these models for determining basic relationships among materials morphology, properties in key performance indices including cycling rate and electrode particle size, diffusivity, and electronic conductivity on the specific energy and specific power.

Thus, in this study, we seek to use cell simulations in conjunction with surrogate-based analysis tools to examine the effect of cycling rate and cathode particle size, diffusivity, and electronic conductivity on the specific energy and specific power capability. Since the mean and maximum cycling rates for a battery can be estimated from its expected application, these results can be used as guidelines for electrode design optimization.

2. Methodology

2.1. Battery simulation model

In this study, the galvanostatic discharge of a cell consisting of negative electrode–separator–positive electrode (Fig. 1) has been modeled using the porous-electrode formulation [12]. Porous-electrode models solve the continuum scale governing equations for predicting the cell performance under various operating conditions. The porous-electrode formulation has been shown to include the physiochemical processes involved in the cell, which the equivalent circuit approach fails to take into account. Since the former

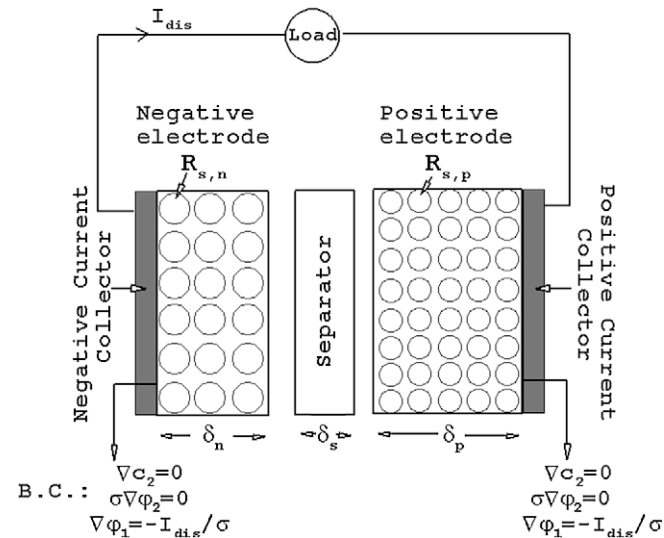


Fig. 1. Lithium-ion cell model showing spherical electrode particles and boundary conditions.

are based on homogenization, the detailed microstructure cannot be considered in the analysis, and hence effective material properties employ empirical models. In the porous-electrode model, movement of lithium ions from the negative (anode) to the positive (cathode) electrode is described through transient one-dimensional transport equations as follows.

In the solid, diffusion inside spherical particles is considered to be the mechanism for transport of lithium, and can be described as:

$$\frac{\partial c_1}{\partial t} = D_s \left(\frac{\partial^2 c_1}{\partial r^2} + \frac{2}{r} \frac{\partial c_1}{\partial r} \right) \quad (1a)$$

with boundary conditions:

$$\frac{\partial c_1}{\partial r} = 0 \quad \text{at } r = 0 \quad (1b)$$

$$\frac{i_{n,j}}{F} = -D_s \frac{\partial c_1}{\partial r} \quad \text{at } r = R_{s,j} \quad (1c)$$

where $j = n$ (anode) or p (cathode).

In the liquid electrolyte:

$$\varepsilon \frac{\partial c_2}{\partial t} = \nabla \cdot (D_2^{\text{eff}} \nabla c_2) - \frac{s_i}{n} \frac{1-t_+^0}{F} \nabla \cdot i_2 - \frac{i_2 - \nabla t_+^0}{F} \quad (2)$$

with the boundary conditions shown in Fig. 1 [12,17]. In Eqs. (1) and (2), c_1 and c_2 denote the lithium-ion concentrations in the solid and liquid phases, respectively. The initial concentration in the electrolyte was chosen to be $c_2 = 1000 \text{ mol/m}^3$. A gradient of the chemical potential is the driving force for the lithium-ion diffusion across the width of the cell. In the existing model, the chemical kinetics at the particle–electrolyte interface is described using the Butler–Volmer equation, in which the flux on the particle surface is a function of the exchange current density and the surface overpotential, as shown in the following equation:

$$i_{n,j} = i_{0,j} \left[\exp \left(\frac{\alpha_{a,j} F}{RT} \eta_j \right) - \exp \left(-\frac{\alpha_{c,j} F}{RT} \eta_j \right) \right] \quad (3)$$

where the exchange current density is given by the following equation:

$$i_{0,j} = Fk(c_1)^{\frac{1}{2}}(c_2)^{\frac{1}{2}}(c_{1,\text{max}} - c_1)^{\frac{1}{2}} \quad (4)$$

and $\eta_j = \varphi_1 - \varphi_2 - U_{\text{OCP}}$ is the surface overpotential. The surface overpotential on the positive electrode is estimated based on the open-circuit potential given in Eq. (5), and the electrical potentials in the solid (φ_1) and liquid (φ_2) phases, using Eqs. (6) and (7):

$$U_{\text{OCP}} = 4.06279 + 0.0677504 \tan h(12.8268 - 21.8502y) - 0.105734 \left[-1.575994 + (1.00167 - y)^{0.379571} \right] - 0.045e^{-71.69y^8} + 0.01e^{-200(y-0.19)} \quad (5)$$

$$\nabla \cdot (\sigma \nabla \varphi_1) - J = 0 \quad (6)$$

$$\nabla \cdot (\kappa \nabla \varphi_2) + \nabla \cdot (\kappa_D \nabla (\ln c_2)) + J = 0 \quad (7)$$

where $J = \nabla \cdot i_2$ is the volumetric reaction current in the electrolyte,

$$\kappa_D = (1 - t_+^0) \frac{\kappa RT}{F} \left(1 + \frac{\partial \ln f_a}{\partial \ln c_2} \right) \quad (8)$$

$$J = \begin{cases} \left(\frac{3\varepsilon_1}{R_s} \right)_p i_{n,p} & \text{in the positive electrode} \\ 0 & \text{in the separator} \\ \left(\frac{3\varepsilon_1}{R_s} \right)_n i_{n,n} & \text{in the negative electrode} \end{cases} \quad (9)$$

and $\varepsilon_{1,p}$ ($\varepsilon_{1,n}$) and $R_{s,p}$ ($R_{s,n}$) are the porosity and particle size in the positive (negative) electrode, respectively. More details of the

formulation can be found in Refs. [12,23,24]. An important advantage of the battery model is that the simulations are computationally inexpensive, with typical case runtimes on the order of a few minutes or less. This allows for simulating a large number of cases to probe the wide design ranges considered in this study.

2.2. Surrogate models

Surrogate models can be used to predict the behavior of an objective function (in this case the battery energy or power) within the design space based on data obtained from simulations at selected design points. Surrogate models can be categorized in two groups, namely parametric (e.g. PRS, KRG) and non-parametric (e.g. RBNN). Different types of surrogate models should be attempted and compared, since the best method is problem-dependent and cannot be predicted beforehand. A brief description of the commonly used models is as follows; further details can be found in Ref. [25]. The key steps in the surrogate modeling process are shown in Fig. 2.

2.2.1. Polynomial response surface (PRS)

In a polynomial response surface model, the objective function is approximated as a linear combination of polynomial basis functions:

$$\hat{y}(x) = \sum_i b_i f_i(x) \tag{10}$$

The number of i terms and the maximum degree of $f_i(x)$ are determined by the order of the PRS model. There often exists an “optimum” polynomial order; higher-order polynomial response surfaces can potentially achieve greater accuracy by allowing more degrees of freedom, but can also suffer from excessive curvature that can hinder accuracy and show inconsistent trends in the objective function from actual data. The coefficient vector \mathbf{b} is selected using a least squares method such that the prediction error at the training data points is minimized.

The adjusted coefficient of multiple determinations quantifies the prediction capability of the polynomial response surface approximation. This parameter is defined as

$$R_{adj}^2 = 1 - \frac{\sigma_a^2(N_s - 1)}{\sum_{i=1}^{N_s} (y_i - \bar{y})^2} \tag{11}$$

where \bar{y} is the mean value of the objective function y at the data points and σ_a is the RMS error of the polynomial response surface at the data points. A good polynomial fit should have a small RMS error, and thus an R_{adj}^2 value close to 1.

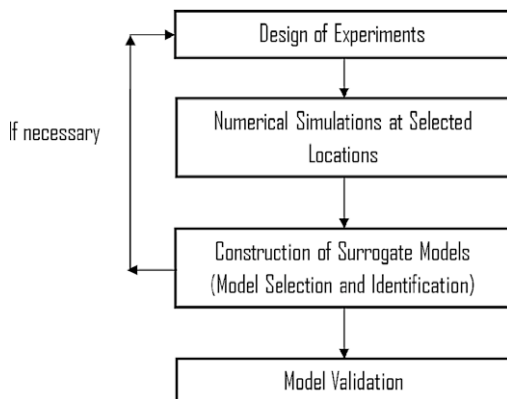


Fig. 2. Flowchart for the surrogate-based modeling framework [25].

2.2.2. Kriging (KRG)

A kriging implementation by Lophaven et al. [26] is used in this study. The objective function $y(x)$ is approximated as a sum of a polynomial regression model and a systematic departure $Z(x)$:

$$y(x) = \hat{y}(x) = \sum_i b_i f_i(x) + Z(x) \tag{12}$$

The systematic departure components are assumed to be correlated as a function of distance between the locations under consideration. In this study, a variety of correlation functions are considered: Gaussian, linear, exponential, cubic, spline, and spherical. A detailed formulation of these correlation functions has been summarized by Lophaven et al. [26].

2.2.3. Radial-basis neural network (RBNN)

A radial-basis neural network model approximates the objective function as a linear combination of N_{RBF} radial-basis functions [27], also known as neurons:

$$\hat{y}(x) = \sum_{i=1}^{N_{RBF}} w_i a_i(x) \tag{13}$$

The Gaussian function has been used as the radial-basis function in this study:

$$a_i(x) = e^{-\frac{\|s_i - x\|^2}{\rho^2}} \tag{14}$$

where the quantity $\|s_i - x\|$ is the distance to the i th radial-basis function. The number of neurons and associated weights are determined by satisfying the user defined error “goal” on the mean squared error in approximation.

2.3. Cross-validation

In order to select appropriate surrogate models for analysis, methods for evaluating and comparing the accuracy of the models are required. Procedures for comparing error measures for kriging and PRS models have been developed by Goel et al. [28]. One strategy used in this study was to obtain simulation data at test points not used in the construction of surrogate models. The prediction error could then be computed at each test point for each surrogate model. While this method is easy to use and is useful for performing cross-validation, it is also limited by the number of test points that can be selected and the location of these points. The use of other cross-validation techniques in conjunction with test-point prediction error has also been adopted.

To estimate the accuracy of a surrogate model independent of test points, a parameter called the prediction error sum of squares (PRESS) can also be computed. PRESS is computed directly from the training data by summing the “leave-one-out” prediction errors at all data points. The “leave-one-out” prediction error is defined as the prediction error at a particular point using the surrogate model constructed from all other data points. In a more general formulation allowing an arbitrary number of data points to be left out at a time, this parameter is known as the generalized mean square error (GMSE). In this study, we use the RMS PRESS value as the basis of evaluation and comparison:

$$RMS\ PRESS = \sqrt{\frac{1}{N} \sum_{i=1}^{N_s} (y_i - \hat{y}_i^{(-i)})^2} \tag{15}$$

where $\hat{y}_i^{(-i)}$ represents the prediction at $\mathbf{x}^{(i)}$ using the surrogate constructed using all sample points except $(\mathbf{x}^{(i)}, y_i)$ [25].

2.4. Global sensitivity analysis

Global sensitivity analysis can be useful for comparing the relative magnitude of effect of the design variables on the objective function, especially if the number of design variables is large. Variables that have little effect on the objective function can be identified and removed from consideration, allowing the design space to be reduced. A method similar to that used by Sobol [29] has been employed in this work.

An objective function f (obtained from the surrogate model) can be decomposed as a sum of functions of individual variables and combinations of variables, known as additive functions:

$$f(x) = f_0 + \sum_i f_i(x_i) + \sum_{i<j} f_{ij}(x_i, x_j) + \dots + f_{1-N_p}(x_1, \dots, x_{N_p}) \quad (16)$$

The total variance $V(f)$ is defined as the expected value of the square of the summation of all non-zero order additive functions. The total variance can also be expressed as a sum of partial variances of the individual variables and combinations of variables:

$$V(f) = \sum_{i=1}^{N_p} V_i + \sum_{i<j} V_{ij} + \dots + V_{1-N_p} \quad (17)$$

The partial variances are in turn defined in terms of the expected value of the additive functions:

$$\begin{aligned} V_i &= V(E[f|x_i]) \\ V_{ij} &= V(E[f|x_i, x_j]) - V_i V_j \\ &\dots \end{aligned} \quad (18)$$

The expected values of the additive functions and their variances can be expressed as integrals of the additive functions that can be approximated using Gauss-quadrature or Monte-Carlo methods:

$$E[f|x_i] = \int_0^1 f_i dx_i \quad (19a)$$

$$V(E[f|x_i]) = \int_0^1 f_i^2 dx_i \quad (19b)$$

In this study, a 5-point Gauss-quadrature integration scheme is used. The main sensitivity indices can then be computed from the partial variances:

$$S_{Mi} = \frac{V_i}{V(f)} \quad (20)$$

The total sensitivity index for the i th variable is defined as the sum of all variance terms involving i , divided by the total variance. This can be expressed as a sum of the main sensitivity index and all higher-order terms involving i :

$$S_{Ti} = S_{Mi} + \frac{\sum_{j \neq i} V_{ij} + \dots}{V(f)} \quad (21)$$

The relative importance of the design variables can be observed by comparing either their partial variances (main sensitivity indices) or their total variances (total sensitivity indices). The difference between the main and total sensitivity indices for each variable also gives an indication of the degree of interaction between variables.

2.5. Pareto-optimal front

A single objective can be optimized by simply searching the design space for the minimum or maximum value of the objective. However, if multiple competing objectives are present, such as specific power and specific energy, there may be no single optimal design, but many designs in which one objective is improved at the cost of another [30]. Pareto-optimal solutions (also known as Pareto-efficient solutions) are designs that are not dominated by any

other design. A design is said to be dominated by another if it is no better in all objectives, and worse in at least one objective. The set of Pareto-optimal solutions can be used to construct a Pareto-optimal front, which represents all optimal combinations of the objectives if their relative importance is not known. In this study, both specific energy and specific power are considered as objectives.

3. Results and discussion

The focus of this study is on the positive electrode (cathode), so the design variables (particle size, diffusivity, conductivity) apply only to the cathode material. The design variables studied and their ranges are summarized in Table 1. The discharge rate range was selected to cover typical power requirements in automotive applications. In addition, high power and high energy applications require thin ($\sim 10 \mu\text{m}$) and thicker ($\sim 100 \mu\text{m}$) electrodes, respectively. Since the electrode can be assumed to be composed of multiple layers, the particle size range was chosen to be an order of magnitude lower than the electrode thicknesses. The selected particle size range is also consistent with that found in real electrodes [31,32].

For a macroscopic model, the effective transport properties are needed to solve the governing equations. The numerical method employed uses the Bruggeman's equation to quantify the effective conductivity based on the volume fraction of the liquid electrolyte. On the other hand, the microscopic diffusion equation is solved for the solid particles, which uses the intrinsic diffusion coefficient. Data reported in the literature for transport properties, such as diffusivity of the solid and electrical conductivity, varies substantially as a result of experimental uncertainty, differences in electrode microstructure, as well as phase changes due to different states of charge, and differences in measurement techniques [4,16]. For instance, the reported values for the diffusion coefficient vary between $1.4 \times 10^{-14} \text{ m}^2/\text{s}$ [33] and $4.89 \times 10^{-13} \text{ m}^2/\text{s}$ [34] for MnO_2 electrodes whereas the electrical conductivity varies from 3.8 S/m [10] to 100 S/m [22]. While the intrinsic values of the transport properties of homogeneous materials are fixed under given thermodynamic conditions, it is known [35,36] that values of the "effective" transport properties for materials of complex microstructural compositions depend on geometric characteristics as well as the operating conditions. As a result, the diffusion coefficient and electrical conductivity ranges in the current study have been chosen to (a) cover this order of magnitude difference in the earlier reported values, and (b) span a suitable range to account for the geometric characteristics of the electrode. The materials and various parameters of the electrodes considered in this study are summarized in Table 2.

The electrolyte considered is LiPF_6 in EC:DMC (a mixture of ethylene carbonate and dimethyl carbonate in 1:1 ratio by weight). The current collectors were aluminum and copper foil for the anode and cathode, respectively, and had a thickness of 25 μm each. The separator thickness was also 25 μm . The specific energy provided during the discharge process is obtained by time-integrating the power (the product of the variable voltage and constant current) and normalizing by the total mass. The specific power is

Table 1
Design variables and ranges.

Variable	Symbol	Minimum	Maximum
Cycling rate	C	0.1 C	4 C
Particle radius	$R_{s,p}$	0.2 μm	20 μm
Diffusivity	D_s	$0.1 \times 10^{-13} \text{ m}^2/\text{s}$	$10 \times 10^{-13} \text{ m}^2/\text{s}$
Electrical conductivity	σ	1 S/m	100 S/m

Table 2
Electrode materials and parameters.

Parameter	Cathode	Anode
Material	$\text{Li}_y\text{Mn}_2\text{O}_4$	MCMB 2528 graphite
Thickness	100 μm	100 μm
Initial stoichiometric parameter	0.2	0.495
Porosity	0.3	0.3
Inert filler volume fraction	0.2	0.1
Particle radius	Variable	10 μm
Diffusivity	Variable	$5.0 \times 10^{-13} \text{ m}^2/\text{s}$
Electrical conductivity	Variable	100 S/m

obtained by normalizing the time-averaged power. A cut-off voltage of 2.0 V was selected as the termination criterion for the simulations, in accordance with actual battery cycling in which deep discharge is avoided as it leads to permanent loss of performance due to irreversibility in the electrochemical reactions.

3.1. 4-Variable analysis and order reduction

To construct high fidelity surrogate models for the four design variables considered in this study, a large number of numerical experiments would be essential which may result in an inefficient and time consuming analysis. Instead, it is worthwhile to examine their impact within the selected range. Preliminary simulations were run for cases in which one design variable was varied from its minimum to maximum value, while the values of the other three design variables were fixed. It was observed that varying the electrical conductivity by two orders of magnitude had negligible effect on the specific energy, for all combinations of values for the other variables. Test points were selected to verify that there were no interactions between the variables in the remainder of the design space, which may not have been captured at the extrema. As a result, the number of design variables was reduced by removing conductivity from future consideration, and a constant value of $\sigma = 10 \text{ S/m}$ was used for future simulations.

3.2. 3-Variable surrogate model analysis and validation

For the 3-variable surrogate models, all three model types discussed in the methodology (PRS, RBNN, kriging) were considered. All polynomial orders from 2 to 6 were considered for the PRS models, and multiple correlation function types were considered for the kriging models. Spread coefficients for the RBNN models were varied over a considerable range to find a rough optimum. An initial design of experiments (DOE) of 50 design points consisting of a combination of 15 face-centered central composite (FCCD) and 35 Latin hypercube sampling (LHS) points [37] was selected for simulations and model construction. It was found that of all the surrogate models constructed, the kriging model had the lowest RMS PRESS value, which was over 20%. Of the 50 training data points used to construct the surrogate model three outliers occurred in the region with high cycling rate, large particle size, and low diffusivity, where a sharp gradient in the specific energy was observed. This sparsely populated “critical” region was populated by refining the domain such that an additional 100 design points were added to the original DOE; the additional points were primarily but not exclusively concentrated in the ‘critical’ region. This was accomplished by transforming the design variables to a logarithmic space (base-10 log was used in this case), selecting a design of experiments using LHS, and transforming the variables back to their original form. Such a transformation leads to a narrowed design space (in shrunk log-space), which on back-transformation results in stretching such that the density of points near one extreme is higher than the other.

Using a kriging model constructed from data of this refined DOE, the mean prediction error for nine test points in the “critical” region was reduced to 3.9% from 29.8% for the original DOE. An additional six test points were selected in the entire design space using LHS. The best individual surrogate models were the third- and fourth-order polynomial response surfaces, both with an RMS PRESS value of over 10%, whereas the best kriging model had RMS PRESS of over 100%. The differing performance in the “critical” region and the rest of the design space suggests a shift in fidelity as a result of the domain refinement.

An additional 165 points were selected with LHS in an attempt to improve overall surrogate model accuracy in the entire design space. Combined with the initial design of experiments and the first refinement, a total of 315 points were used in the most-refined design of experiments, of which about 100 points were concentrated in the “critical” region and the remaining 215 distributed throughout the entire design space. A total of 13 individual surrogates including multiple kriging, radial-basis neural network, and polynomial response surface models were considered.

For validation, a total of 64 test points were selected in a full factorial arrangement, in order to evaluate the surrogate model performance in the entire design space. The relative prediction error definition was modified slightly by normalizing the absolute error by a constant value, taken to be the mean value of all test data points:

$$E = \frac{|x_{\text{model}} - x_{\text{data}}|}{\bar{x}_{\text{data}}} \quad (22)$$

This formulation helps avoid deceptively large errors due to large variation in the values of the test data. A comparison among different types of surrogate models revealed that the best kriging model, with a mean prediction error of 2.5% and RMS PRESS of 3.0% with the spline correlation model and first-order polynomial regression, performed better than any radial-basis neural network or polynomial response surface, which was considered satisfactory to perform additional analysis.

3.3. Global sensitivity analysis and design space splitting

Global sensitivity analysis was performed on the 13 surrogate models to compare the relative importance of the design variables and identify any variables that could be eliminated. Similar results were found among models of the same type. The results from all models consistently indicated that none of the three design variables could be ignored.

In addition to the global sensitivity analysis, local sensitivity analysis was also performed on subsets of data to examine the relative effect of the design variables within the corresponding sub-regions of the design space. A comparison of the main and total sensitivity indices computed using surrogate models constructed from data within selected ranges of the diffusion coefficient is shown in Fig. 3(a) and (b), respectively. As shown by the total sensitivity indices in Fig. 3, cross-interactions were especially pronounced in the low diffusivity range. It can be seen that the effect of diffusivity vanishes above some critical value of about $D_{s,\text{crit}} = 10^{-13} \text{ m}^2/\text{s}$. This is consistent with what may be expected as the diffusivity is increased: eventually a critical point would be reached where the allowable diffusion rate exceeds that required by the discharge process, beyond which further increases to the diffusion coefficient would not affect the diffusion rates in the battery. Although the role of diffusion coefficient has been investigated [12,14,16,19], its relative importance under different rate and particle size scenarios has not been established. Considering the difficulty of modeling the entire design space with a single surrogate model, the sensitivity analysis results present an opportunity to split the design space along this critical value. This

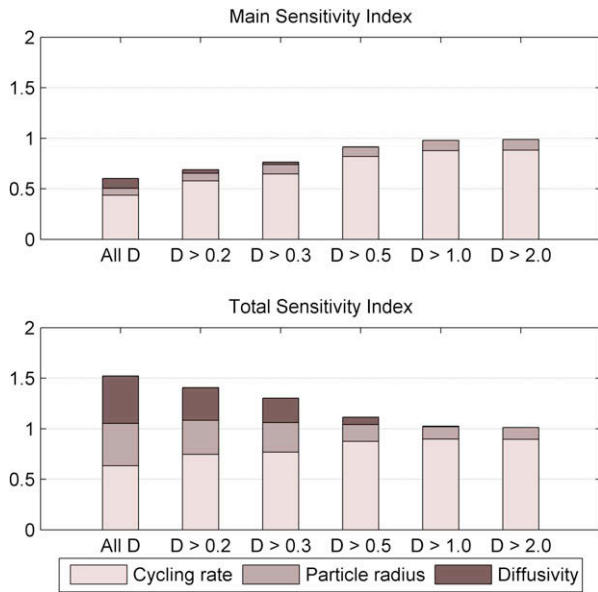


Fig. 3. Sensitivity indices for selected diffusivity ranges with kriging model; D_s in units of $10^{-13} \text{ m}^2/\text{s}$.

splitting of the design space along $D_{s,\text{crit}}$ results in a narrower range of diffusivity values below the critical value to be considered in the 3-variable study, which may allow for faster and more accurate surrogate model prediction. Above the critical value, the diffusivity can be removed from consideration due to its negligible effect on the specific energy, resulting in a reduced-order 2-variable problem. While narrowing the diffusivity range for the 3-variable study was helpful, some difficulties remained: the design variables varied over at least one order of magnitude and the specific energy value spanned a large range. The analysis was further simplified by introducing a dimensionless time parameter, τ :

$$\tau = \frac{\tau_{\text{dis}}}{t_{\text{dif}}} \quad (23)$$

This dimensionless time can be used to compare the relative rates of the discharge and diffusion processes, which previous results have suggested are the main determinants of the energy storage. This approach adopted is similar to Ref. [16], where the ratio of the solid-diffusional resistance and the interfacial kinetic resistance was used to identify the diffusion-limited intercalation process. In this formulation, t_{dis} is the discharge time required to reach termination, by reaching either the cut-off voltage or complete state of discharge. t_{dif} is a characteristic diffusion time which is defined based on the particle size and diffusion coefficient:

$$t_{\text{dif}} = \frac{R_{s,p}^2}{D_s} \quad (24)$$

For the current design of experiments, τ varies across several orders of magnitude, from cases where the diffusion time is much longer than the discharge time (diffusion-limited cases) to where diffusion time is much shorter than the discharge time (diffusion-independent cases). A plot of specific energy against dimensionless time is shown in Fig. 4, where the dimensionless time was only computed for the range $D_s < 10^{-13} \text{ m}^2/\text{s}$.

Two distinct dimensionless time ranges can be identified in Fig. 4. In the low τ range, i.e. $D_s < 10^{-13} \text{ m}^2/\text{s}$ (left of the dotted line), the specific energy increases monotonically with increasing τ ; this can be considered a 'diffusion-limited' region since the energy is limited by the allowable diffusion rate. In the high τ range (right of the dotted line), the scatter in the specific energy values

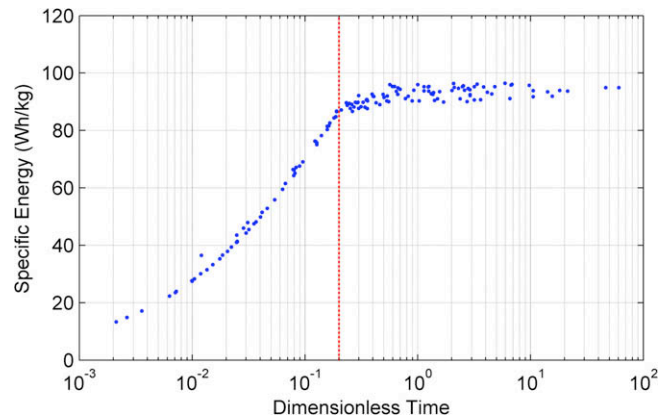


Fig. 4. Specific energy capacity vs. dimensionless time for $D_s < 10^{-13} \text{ m}^2/\text{s}$.

indicates that diffusion is no longer the sole determining factor. This can be considered an 'intermediate' region between the diffusion-limited ($D_s < 10^{-13} \text{ m}^2/\text{s}$) and 'diffusion-independent' ($D_s \geq 10^{-13} \text{ m}^2/\text{s}$) regimes. Based on this observation, the design space for $D_s < 10^{-13} \text{ m}^2/\text{s}$ can be further split, as it can be observed from Fig. 4 that the variation of energy in the diffusion-limited region can be effectively captured with a single-variable model. Zhang et al. [16] have also shown that for fast interfacial kinetics the intercalation process is diffusion-limited, although the critical value where it ceases to be dependent on the diffusion coefficient was not evaluated. The current results are also found to be consistent with earlier two-dimensional simulations [19], which show that the total capacity and power density of the battery diminish with decreasing diffusivity. The complete 3-variable design space has thus been divided into three sub-regions for separate analysis, and the overall process has been shown in Fig. 5. For low diffusivities the ratio of the discharge to diffusion time scales captures the specific energy that could be derived from the Li-ion cell. On the other hand, the original three variable problem of predicting battery energy storage reduces to a 2-variable dependence for diffusivities higher than $10^{-13} \text{ m}^2/\text{s}$. The 'intermediate' region, as shown in Fig. 5, bridges the gap between the diffusion-limited and the diffusion-independent regimes, where the specific energy is a function of discharge rate, particle size and diffusivity of the solid.

As shown in Fig. 6, surrogate models were constructed on each of the partitioned design sub-regions. Since the design space was split but not expanded, no new training data were required.

The diffusion-limited region was modeled by a single-variable curve fit due to the monotonic relationship observed in Fig. 4 for $\tau < 0.2$. Since the relationship between the specific energy and the dimensionless time parameter was non-linear, a fourth-order polynomial surface with $R_{\text{adj}}^2 = 0.994$ was fitted to the data, as shown in Fig. 6(a). The non-linear behavior may be attributed to an increasing contribution from the intermediate and diffusion-independent regions as the dimensionless time parameter is increased, combined with the zero-diffusivity limit where the total energy is expected to be zero.

Although the intermediate region retains full dimensionality, the ranges of the design variables are reduced, and model accuracy is improved considerably. As seen in Fig. 6(b), the specific energy decreases considerably with increasing cycling rate and particle size, while the effect of diffusivity is reduced. The effect of diffusivity is weaker than in the diffusion-limited region since the material is sufficiently diffusive to allow interplay between the design variables as well as with other factors such as the fixed electrolyte and anode properties, but not so diffusive that the cell performance becomes independent of the diffusion coefficient. For model valida-

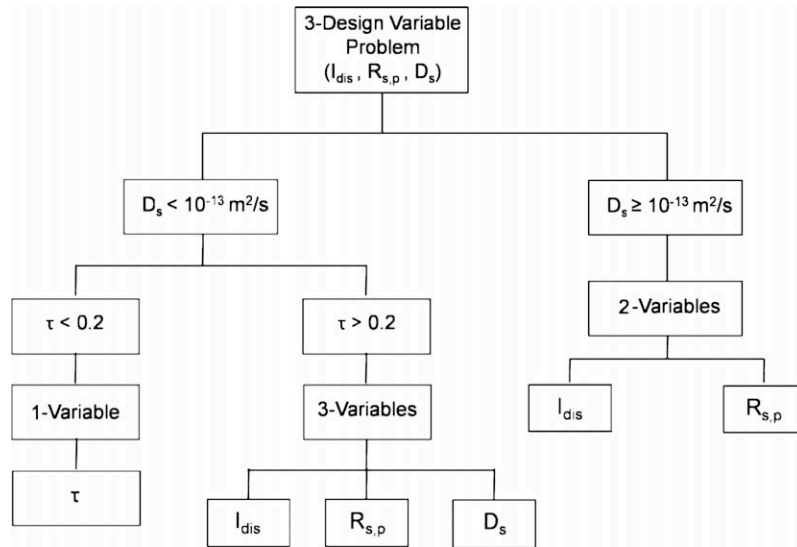


Fig. 5. Overall process to split the original 3-design variable problem into three distinct regimes using sensitivity analysis and based on a critical value of the diffusion coefficient, i.e. $D_{s,crit} = 10^{-13} \text{ m}^2/\text{s}$.

tion, 10 test points were selected such that their distances to training data points were maximized. Excellent agreement between surrogate model prediction and test data was achieved with a variety of models. The lowest RMS PRESS value (0.40%) was achieved with a Gaussian correlation kriging model, although a third-order polynomial surface had better prediction at test points (mean error 0.22% vs. 0.30%).

In the diffusion-independent regime, only the cycling rate and particle radius have a significant effect because the diffusion coefficient exceeds the required value to provide the necessary ion transport rate. A reduced-order 2-variable surrogate model was constructed to fit the data in the range $D_s > 10^{-13} \text{ m}^2/\text{s}$, and is shown in Fig. 6(c). A kriging model with spherical correlation was employed with an RMS PRESS value of less than 1.4%, which was considered satisfactory for model construction. For the purpose of further cross-validation, the diffusion coefficient was varied while keeping the cycling rate and particle size fixed. Increasing the diffusion coefficient by a factor of 2 did not lead to a difference in the specific energy by more than 0.1%.

3.4. Energy-power trade

Results so far have focused exclusively on the specific energy capacity as the objective function, since that tends to be the most critical limitation on battery performance in a variety of applications. However, specific power can also be of great importance in applications such as power tools and electric vehicles. Based on Ohm's law, the power can be expected to depend linearly on the cycling rate, since the power varies linearly with discharge current which in turn varies linearly with the cycling rate (by definition). The competing effects of this increase in specific power with increasing cycling rate and the previously observed decrease in specific energy with increasing cycling rate form a multi-objective optimization problem, for which a Pareto-optimal front can be constructed. Additional specific energy and specific power data was generated from randomly sampled design points and earlier constructed surrogate models to obtain a clearly identifiable Pareto-optimal front. Specific energy data were obtained using the split design space approach shown in Fig. 5. For generating specific power data, a separate fourth-order polynomial response surface model was constructed which had an RMS PRESS value of less than 0.4% and R_{adj}^2 of over 0.9999. A plot of specific power against spe-

cific energy for all design points is shown in Fig. 7, along with the Pareto-optimal front.

Since the specific power was expected to be linearly dependent on the cycling rate, the Pareto inefficiency for the majority of designs was expected to be due to the other design variables. This was verified by selecting three cases at a fixed cycling rate but at different particle sizes and diffusivities, which are highlighted with a different color¹ in Fig. 7. In the three cases, the power level was approximately the same, confirming the dependence of the specific energy on only the cycling rate. The specific energy was also found to be lower for larger particle radius and lower diffusion coefficient, which is consistent with the results found previously. The front shows stiffness in favor of high power, which can be achieved with relatively little sacrifice in energy. However, a greater amount of scatter in the specific energy data can also be observed as the specific power is increased. This suggests that the cell performance becomes increasingly sensitive to the other design variables as the cycling rate is increased, resulting in a greater penalty for large particle size or low diffusivity in the cathode. These results are in agreement with [10], where it was shown that at higher discharge rates even a small change in the solid diffusion coefficient could lead to significant changes in the discharge profile.

4. Summary and conclusions

In this study, a physics-based model for Li-ion battery cells consisting of porous electrodes was used to create scalable models that are capable of incorporating both materials properties and morphology into simulations of battery performance. Surrogate-based tools were used to construct and validate models capable of predicting the specific energy and specific power of a lithium-ion battery cell, given the cycling rate and cathode particle size, diffusivity, and electrical conductivity. It was observed that the available energy decreases with faster cycling rate, larger particle size, and low diffusivity. The negligible influence of the electrical conductivity of the cathode material was also demonstrated, and can thus be ignored in practice as long as the value lies within the design range considered. The trends in the cycling rate, particle

¹ For interpretation of the references to color in Fig. 7, the reader is referred to the web version of this paper.

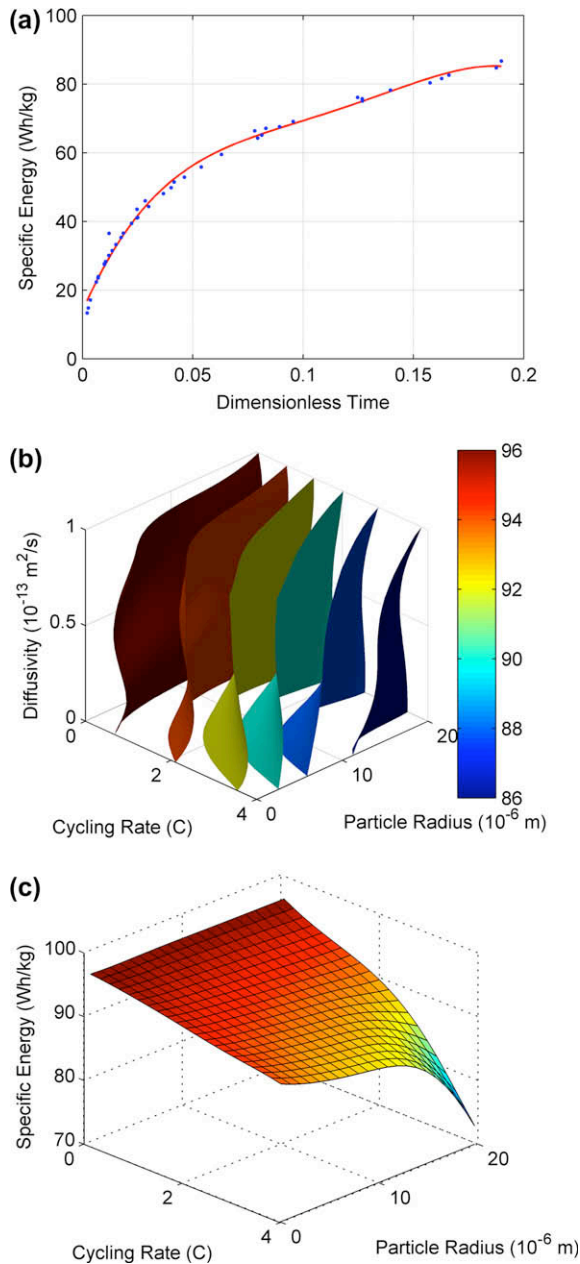


Fig. 6. Specific energy as a function of the design variables for (a) diffusion-limited with fourth-order polynomial curve fit ($R_{\text{adj}}^2 = 0.994$), (b) intermediate, with 3-design variables, and (c) diffusion-independent regions shown.

size, and diffusivity suggested a link between the relative discharge and diffusion rates and the energy storage of the cell, which was quantified in terms of the discharge and diffusion time scales. Surrogate models were also used to construct a Pareto-optimal front which showed stiffness in favor of high power, but also greater sensitivity to design variables at high power levels. The surrogate models developed in this study provide a framework for assessing the competition between multiple variables and objectives. Although the effects of particle size, diffusivity, and rate on battery performance have been studied previously, our approach allows for quantifiable sensitivity analysis under different scenarios, and improved understanding of the global parameter space beyond case studies. A global assessment of the interplay of the various input variables, namely, the particle size, diffusivity, and rate, and their ranked order of importance in relation to the objectives is more clearly established in the current framework. Additionally,

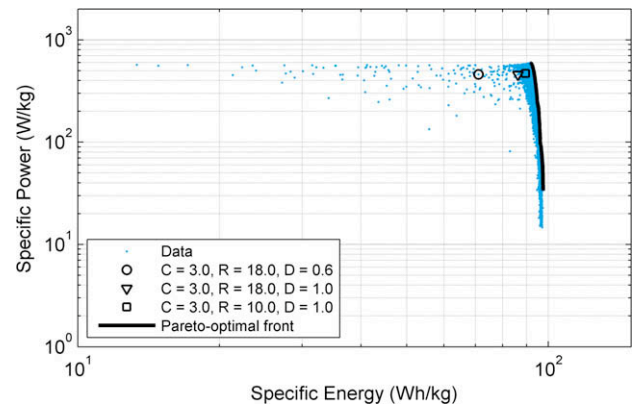


Fig. 7. Pareto-optimal front for specific power and specific energy.

although the porous-electrode model used in this study is computationally inexpensive, the surrogate modeling framework can be readily extended to incorporate more detailed battery models, such as that presented in Ref. [38].

It was observed that the presence of large ranges in design variables could lead to non-physical variations in the surrogate models. Large gradient regions are especially difficult to capture, and refinement of design points in the large-gradient region sometimes merely shifts fidelity from one region to another, leading to poor prediction elsewhere. However, by separating the design space based on critical diffusivity and dimensionless time values, independent analysis of reduced-order sub-regions resulted in greatly improved surrogate model prediction. The preferred surrogate model after splitting the design space varied depending on the sub-region. In the diffusion-limited region, a polynomial response surface was best, while two different kriging models were preferable in the intermediate and diffusion-independent regions. For predicting the specific power, a polynomial response surface was selected. The preferred model differs between the regions due to the varying behavior of the objective function.

There are certain limitations to the current methodology that should be addressed. An important simplification in the battery model is the assumption of uniformly sized, spherical particles which prevents the model from accounting for the effects of detailed microstructure (a homogeneous porosity is assumed). Another simplification is the use of fixed material properties throughout the cycle, such as diffusion coefficient and electrical conductivity. While experiments have shown that the diffusion coefficient depends on the state of charge [4,5] and the electrode microstructure, analytical work using particle-scale modeling of the electrodes is being pursued currently to determine these effective material properties in the framework of multiscale modeling, similar to those discussed in [35,36]. Note that although cross-dependencies, such as the dependence of the diffusion coefficient on particle size, are not directly considered, the surrogate models can account for such effects since they map the full design space.

Furthermore, the specific energy capacity values reported in this study are low compared to what has been achieved in real batteries [1]. Since the goal of this study was to understand the physics responsible for the trends in response to the design variables rather than maximize the battery performance, the actual output values were not considered to be of critical importance. Finally, all design variables considered in this study apply only to the positive electrode (cathode), and parameters governing the current collectors, separator, electrolyte, and negative electrode were not optimized. Other parameters for the positive electrode that were not discussed in this study such as the electrode thickness, porosity, and ambient

temperature could also have significant impact on the battery performance and will be examined in a future study.

Acknowledgements

The present efforts have been supported by a Department of Energy and General Motors funded project for the Advanced Battery Coalition for Drivetrains (ABCD).

References

- [1] J.-M. Tarascon, M. Armand, Issues and challenges facing rechargeable lithium batteries, *Nature* 414 (2001) 359–367.
- [2] M. Armand, J.-M. Tarascon, Building better batteries, *Nature* 451 (2008) 652–657.
- [3] J.R. Owen, Rechargeable lithium batteries, *Chem. Soc. Rev.* 26 (1997) 259–267.
- [4] M.D. Levi, D. Aurbach, Diffusion coefficients of lithium ions during intercalation into graphite derived from the simultaneous measurements and modeling of electrochemical impedance and potentiostatic intermittent titration characteristics of thin graphite electrodes, *J. Phys. Chem. B* 101 (1997) 4641–4647.
- [5] J. Barker, R. Pynenburg, R. Koksang, M.Y. Saidi, An electrochemical investigation into the lithium insertion properties of Li_xCoO_2 , *Electrochim. Acta* 41 (1996) 2481–2488.
- [6] C. Ho, I.D. Raistrick, R.A. Huggins, Application of A-C techniques to the study of lithium diffusion in tungsten trioxide thin films, *J. Electrochem. Soc.* 127 (1980) 343–350.
- [7] I. Rubinstein, J. Rishpon, S. Gottesfeld, An AC-impedance study of electrochemical processes at nafion-coated electrodes, *J. Electrochem. Soc.* 133 (1986) 729–734.
- [8] J.L. Shui, G.S. Jiang, S. Xie, C.H. Chen, Thin films of lithium manganese oxide spinel as cathode materials for secondary lithium batteries, *Electrochim. Acta* 49 (2004) 2209–2213.
- [9] R. Yazami, Y. Ozawa, A kinetics study of self-discharge of spinel electrodes in $\text{Li}/\text{Li}_x\text{Mn}_2\text{O}_4$ cells, *J. Power Sources* 153 (2006) 251–257.
- [10] P. Arora, M. Doyle, A.S. Gozdz, R.E. White, J. Newman, Comparison between computer simulations and experimental data for high-rate discharges of plastic lithium-ion batteries, *J. Power Sources* 88 (2000) 219–231.
- [11] B. Haran, B.N. Popov, R.E. White, Determination of the hydrogen diffusion coefficient in metal hydrides by impedance spectroscopy, *J. Power Sources* 75 (1998) 56–63.
- [12] M. Doyle, T.F. Fuller, J. Newman, Modeling of galvanostatic charge and discharge of the lithium/polymer/insertion cell, *J. Electrochem. Soc.* 140 (1993) 1526–1533.
- [13] S. Santhanagopalan, Q. Guo, R.E. White, Parameter estimation and model discrimination for a lithium-ion cell, *J. Electrochem. Soc.* 154 (2007) A198–A206.
- [14] B. Paxton, J. Newman, Variable diffusivity in intercalation materials – a theoretical approach, *J. Electrochem. Soc.* 143 (1996) 1287–1292.
- [15] P. Arora, R.E. White, M. Doyle, Capacity fade mechanisms and side reactions in lithium-ion batteries, *J. Electrochem. Soc.* 145 (1998) 3647–3667.
- [16] D. Zhang, B.N. Popov, R.E. White, Modeling lithium intercalation of a single spinel particle under potentiodynamic control, *J. Electrochem. Soc.* 147 (2000) 831–838.
- [17] G.S. Nagarajan, J.W. Van Zee, R.M. Spotnitz, A mathematical model for intercalation electrode behavior, *J. Electrochem. Soc.* 145 (3) (1998) 771–779.
- [18] M. Doyle, Y. Fuentes, Computer simulations of a lithium-ion polymer battery and implications for higher capacity next-generation battery designs, *J. Electrochem. Soc.* 150 (2003) A706–A713.
- [19] R.E. Garcia, Y.-M. Chiang, W.C. Carter, P. Limthongkul, C.M. Bishop, Microstructural modeling and design of rechargeable lithium-ion batteries, *J. Electrochem. Soc.* 152 (2005) A255–A263.
- [20] X. Zhang, W. Shyy, A.M. Sastry, Numerical simulation of intercalation-induced stress in Li-ion battery electrode particles, *J. Electrochem. Soc.* 154 (2007) A910–A916.
- [21] X. Zhang, A.M. Sastry, W. Shyy, Intercalation-induced stress and heat generation within single lithium-ion battery cathode particles, *J. Electrochem. Soc.* 155 (2008) A542–A552.
- [22] J.I. Madsen, W. Shyy, R.T. Haftka, J. Liu, Response surface techniques for diffuser shape optimization, *AIAA J.* 38 (2000) 1512–1518.
- [23] T.F. Fuller, M. Doyle, J. Newman, Simulation and optimization of the dual lithium ion insertion cell, *J. Electrochem. Soc.* 141 (1994) 1–10.
- [24] M. Doyle, J. Newman, A.S. Gozdz, C.N. Schmutz, J.-M. Tarascon, Comparison of modeling predictions with experimental data from plastic lithium ion cells, *J. Electrochem. Soc.* 143 (1996) 1890–1903.
- [25] N.V. Quiapo, R.T. Haftka, W. Shyy, T. Goel, R. Vaidyanathan, P.K. Tucker, Surrogate-based analysis and optimization, *Prog. Aerosp. Sci.* 41 (2005) 1–28.
- [26] S.N. Lophaven, H.B. Nielsen, J. Sondergaard, DACE – a Matlab kriging toolbox. Version 2.0, Technical Report, IMM-TR-2002-12, Technical University of Denmark, Denmark, August 2002.
- [27] T. Goel, D.J. Dorney, R.T. Haftka, W. Shyy, Improving the hydrodynamic performance of diffuser vanes via shape optimization, *Comput. Fluids* 37 (2008) 705–723.
- [28] T. Goel, R.T. Haftka, W. Shyy, Comparing error estimation measures for polynomial and kriging approximation of noise-free functions, *Struct. Multidisc. Optim.* 38 (2009) 429–442.
- [29] I. Sobol, Sensitivity estimates for non-linear mathematical models, *Math. Model. Comput. Exp.* 4 (1993) 407–414.
- [30] Y. Mack, T. Goel, W. Shyy, R. Haftka, Surrogate model-based optimization framework: a case study in aerospace design, *Stud. Comp. Intel.* 51 (2007) 323–342.
- [31] J. Cho, Y.J. Kim, B. Park, Novel LiCoO_2 cathode material with Al_2O_3 coating for a Li-ion cell, *Chem. Mater.* (2000) 3788–3791.
- [32] C.-H. Lu, S.-W. Lin, Influence of the particle size on the electrochemical properties of lithium manganese oxide, *J. Power Sources* (2001) 458–460.
- [33] H. Kanoh, Q. Feng, Y. Miyai, K. Ooi, Kinetic properties of a Pt/ λ - MnO_2 electrode for the electroinsertion of lithium ions in an aqueous phase, *J. Electrochem. Soc.* 142 (1995) 702–707.
- [34] H. Kanoh, Q. Feng, T. Hirotsu, K. Ooi, AC impedance analysis for Li^+ insertion of a Pt/ λ - MnO_2 electrode in an aqueous phase, *J. Electrochem. Soc.* 143 (1996) 2610–2615.
- [35] W. Shyy, S.S. Thakur, H. Ouyang, J. Liu, E. Bloosche, *Computational Techniques for Complex Transport Phenomena*, Cambridge University Press, New York, 2005, pp. 235–256.
- [36] E. Sozer, W. Shyy, Modeling of fluid dynamics and heat transfer through porous media for liquid rocket propulsion, *Int. J. Numer. Meth. Heat Fluid Flow* 18 (2008) 883–899.
- [37] M.D. McKay, R.J. Beckman, W.J. Conover, A comparison of three methods for selecting values of input variables in the analysis of output from a computer code, *Technometrics* 21 (1979) 239–245.
- [38] C.-W. Wang, A.M. Sastry, Mesoscale modeling of a Li-ion polymer cell, *J. Electrochem. Soc.* 154 (2007) A1035–A1047.